Chapter 3

Investigation of microstructure and dielectric behavior of $Bi_{2/3}Cu_{3-x}Mg_xTi_4O_{12}$(x=0, 0.05, 0.1 and 0.2) ceramics synthesized by semi-wet route

3.1. Introduction

$ACu_3Ti_4O_{12}$ (where A = Ca,$Y_{2/3}$, $Bi_{2/3}$, $Gd_{2/3}$) type of perovskite oxide was the first time revealed in 1967, [1] which was able to produce high dielectric constant. The detection of ultrahigh dielectric response in body-centered $CaCu_3Ti_4O_{12}$ (CCTO) has induced vast research to understand the underlying physics behind the unusual phenomenon [2-4]. For many technical uses such as condensers, resonators, filters and memory chips, high dielectric materials have been fascinated very much [5-11]. Regularly, the size and execution of such electronic gadgets can be managed by their material properties. Further, the dielectric constant of the material should be independent of temperature and frequency [12]. Recently, high dielectric permittivity ($\varepsilon \sim 10^4$) with weak temperature and frequency-dependent permittivity have been noticed in TiO_2–based ceramics and CCTO ($CaCu_3Ti_4O_{12}$)-like compounds [13, 14]. The search for ultrahigh permittivity ($\varepsilon_r > 10^3$) materials is one of the most popular research topics in the fields of microelectronics and energy storage devices.$CaCu_3Ti_4O_{12}$(CCTO), a typical $ACu_3Ti_4O_{12}$ (ACTO, where A = Ca, Cd, $La_{2/3}$, $Y_{2/3}$, $Bi_{2/3}$, $Na_{1/2}La_{1/2}$, $Na_{1/2}Y_{1/2}$, or $Na_{1/2}Bi_{1/2}$, Sr) ceramic, have been widely studied due to its ultrahigh dielectric permittivity and good frequency/thermal stability. However, other members of the ACTO family with isostructures, have also been widely studied. Impedance spectroscopy estimation shows that the high dielectric study is a direct result of the Internal Barrier Layer Capacitance (IBLC) impact [15-23]. $Bi_{2/3}Cu_3Ti_4O_{12}$ (BCTO) is isostructural with CCTO, already been reported in the literature. It indicated the temperature and frequency dependence of dielectric as CCTO [21-24]. Particles covered with a thin coating of

other materials have improved properties compared to non-functional uncoated particles, such as the $Lu_3Al_5O_{12}$.Ce@SiO_2 core-shell composite, which reduced the thermal/chemical degradation of LEDs [26]. Because of their possible applications in various fields such as engineered multiferroics, catalysts, and biomedical applications, core-shell structured materials have been mostly studied for a few years [25]. The sources of high permittivity in ACTO materials would include extrinsic processes. Some mechanisms have been proposed so far to explain the origin of high dielectric constant and low dielectric loss (tan δ), which eventually help to build up CCTO perovskite material applications. These mechanisms are internal domain, electrode polarization effect, bimodal grain size model, internal barrier layer capacitance (IBLC), and Nano-scale barrier layer capacitance (NBLC) model. An IBLC model, i.e. semi-conducting grains separated by isolating grain boundaries, is currently the most accepted way to explain this phenomenon [27-32]. Polarization at the interfaces of the substance electrodes may also lead to this extrinsic effect [35]. The reasons behind the presence of semiconductivity in the bulk, however, are not yet clear. Cation non-stochiometry mechanism relating to a Cu deficiency in the interior grain area was alleged to responsible for this effect [33-35]. In this present study, We have reported the effects of Mg doping on Cu sites on dielectric properties and Impedance studies of BCTO Ceramic, which was synthesized through the semi-wet method. Its microstructure, dielectric and electric properties were described.

3.2. Materials synthesis and characterizations

$Bi_{2/3}Cu_{3-x}Mg_xTi_4O_{12}$ (where x= 0, 0.05, 0.1, 0.2), referred BCTO, BCMgTO-0.05, BCMgTO-0.1 and BCMgTO-0.2 for x=0, 0.05, 0.1 and 0.2 respectively, were synthesized through semi-wet method .In this technique, chemicals Bismuth nitrate $Bi(NO_3)_3 \cdot 5H_2O$ (99% Merck, India), copper acetate $Cu(CH_3COO)_2 \cdot H_2O$ (99% Merck, India), magnesium acetate $Mg(CH_3COO)_2 \cdot H_2O$ (98.5% Merck, India), and titanium oxide TiO_2 (98.5% Merck, India) starting were used in the stoichiometric ratio. The solution of $Bi(NO_3)_3.5H_2O$, $Cu(CH_3COO)_2 \cdot H_2O$, and $Mg(CH_3COO)_2 \cdot H_2O$ was prepared in distilled water. Solid TiO_2 was added to this solution. The amount of citric acid (99.5%, Merck India)equivalent to metal ion as a chelating agent, was dissolved in distilled water and added to the mixture. The resultant solution was heated on a hotplate magnetic stirrer at 343-353 K to vaporize water permitted for self-ignition. A fluffy mass of BCTO and BCMgTO powders were obtained after the removal of a lot of gasses. Citric acid was also applied as fuel in the ignition step. The resulting BCTO and BCMgTO powders were ground with the help of a pestle and mortar to make a fine powder. The powders were calcined at 1073 K for 6 h. the cylindrical pellets were made with calcined powders using 2% PVA as a binder on applying 5 tons of pressure using hydraulic pressure for 90 s. This binder was burnt out at 773 K for 3 h. Finally, the BCTO and BCMgTO pellets were sintered at 1173 K for 8 h.

The crystalline phase of the sintered samples was identified by using X-ray Diffractometer (MiniFlex2 goniometer, Rigaku, Tokyo, Japan under 30Kv/15mAX-Ray,2θ/θ-continuous scanning mode within the scanning range 20-90°) technique employing CuK_α radiation

(λ=1.54059Å). Bright Field TEM images were obtained by transmission electron microscopy (TEM, FEI Tecnai-20G) with an accelerating voltage of 200 kV. Samples were characterized also by XPS (X-ray Photoelectron Spectroscopy) and SEM (Scanning Electron Microscopy). For dielectric measurements, sintered pellets were polished by silver paste on both sides and dielectric data were taken by LCR meter (PSM 1735-NumetriQ, Newton 4th Ltd.UK) with a variation of temperature (300 K-500 K) and frequency (10^2 Hz-10^7 Hz).

3.3 Results and discussion

3.3.1. X-ray diffraction (XRD) analysis

X-ray diffraction pattern of Mg doped and un-doped BCTO ceramics $Bi_{2/3}Cu_{3-x}Mg_xTi_4O_{12}$(where x=0, 0.05,0.1,0.2) sintered at 1173 K for 8 h is presented in figure 3.1, which clearly shows BCTO phase(JCPDS card no. 46-0725).The main XRD diffraction peaks of BCTO ceramic corresponding to (2 1 1), (2 2 0), (3 1 0), (2 2 2), (3 2 1), (4 0 0), (4 2 2), (4 4 0) planes were found to have the same as CCTO (JCPDS card no. 75-2188).The crystalline size (D) of BCTO and BCMgTO ceramics was determined using the Debye-Scherrer's formula

$$D = \frac{k\lambda}{\beta cos\theta} \qquad (3.1)$$

Where k is the crystal shape coefficient (k=0.89), λ is the wavelength used in XRD, β is the Full-Width Half Maximum (FWHM) and θ is the diffraction angle.

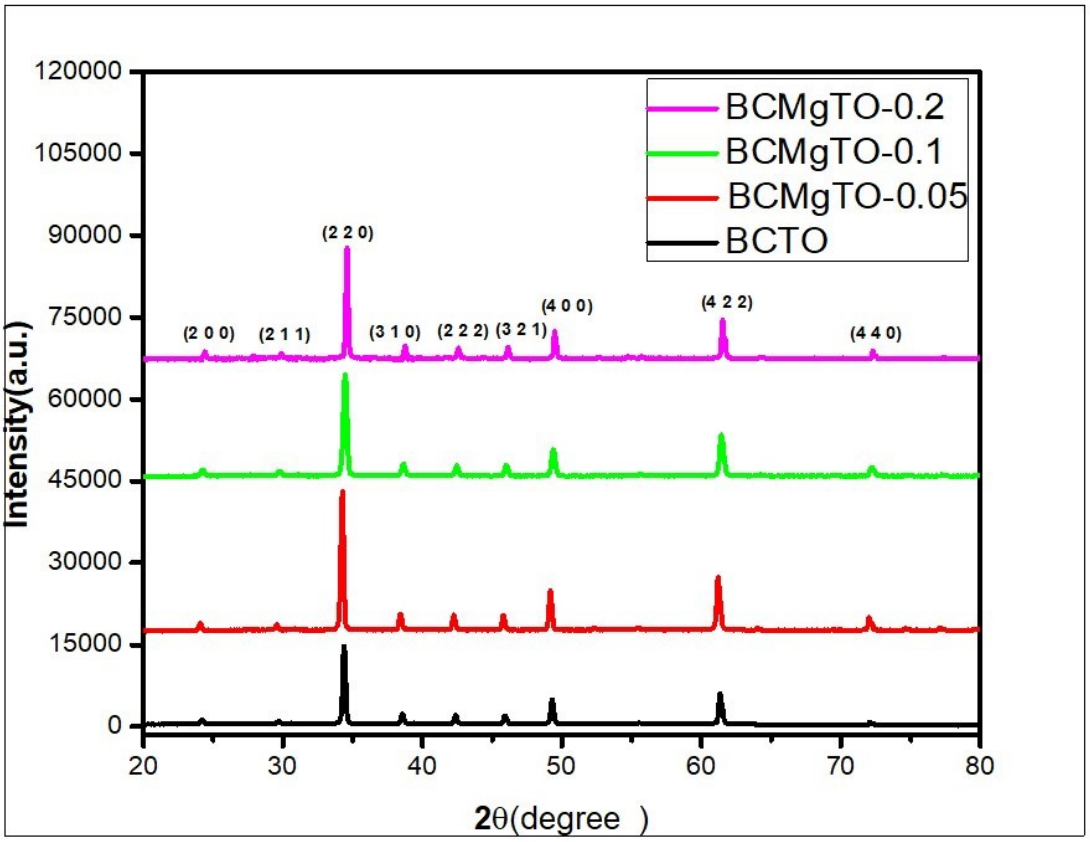

Fig.3.1. XRD Pattern of BCTO, BCMgTO-0.05, BCMgTO-0.1, and BCMgTO-0.2 ceramics sintered at 1173 K for 8 h.

The calculated value of the average crystalline size for BCTO, BCMgTO-0.05, BCMgTO-0.1, and BCMgTO-0.2 ceramics were found to be 35.27 nm, 44.06 nm, 46.70 nm, and 44.72 nm, respectively.

3.3.2. Scanning Electron Microscopic (SEM) studies

SEM images of BCTO, BCMgTO-0.05, BCMgTO-0.1 and BCMgTO-0.2 ceramics is displayed in fig. 3.2a, b, c, and d respectively. The SEM image shows the morphology of

grain and grain boundaries. The average grain size calculated by SEM image of BCTO, BCMgTO-0.05, BCMgTO-0.1, and BCMgTO-0.2 are 0.70 µm, 0.67 µm, 0.63 µm, and 0.56 µm respectively.

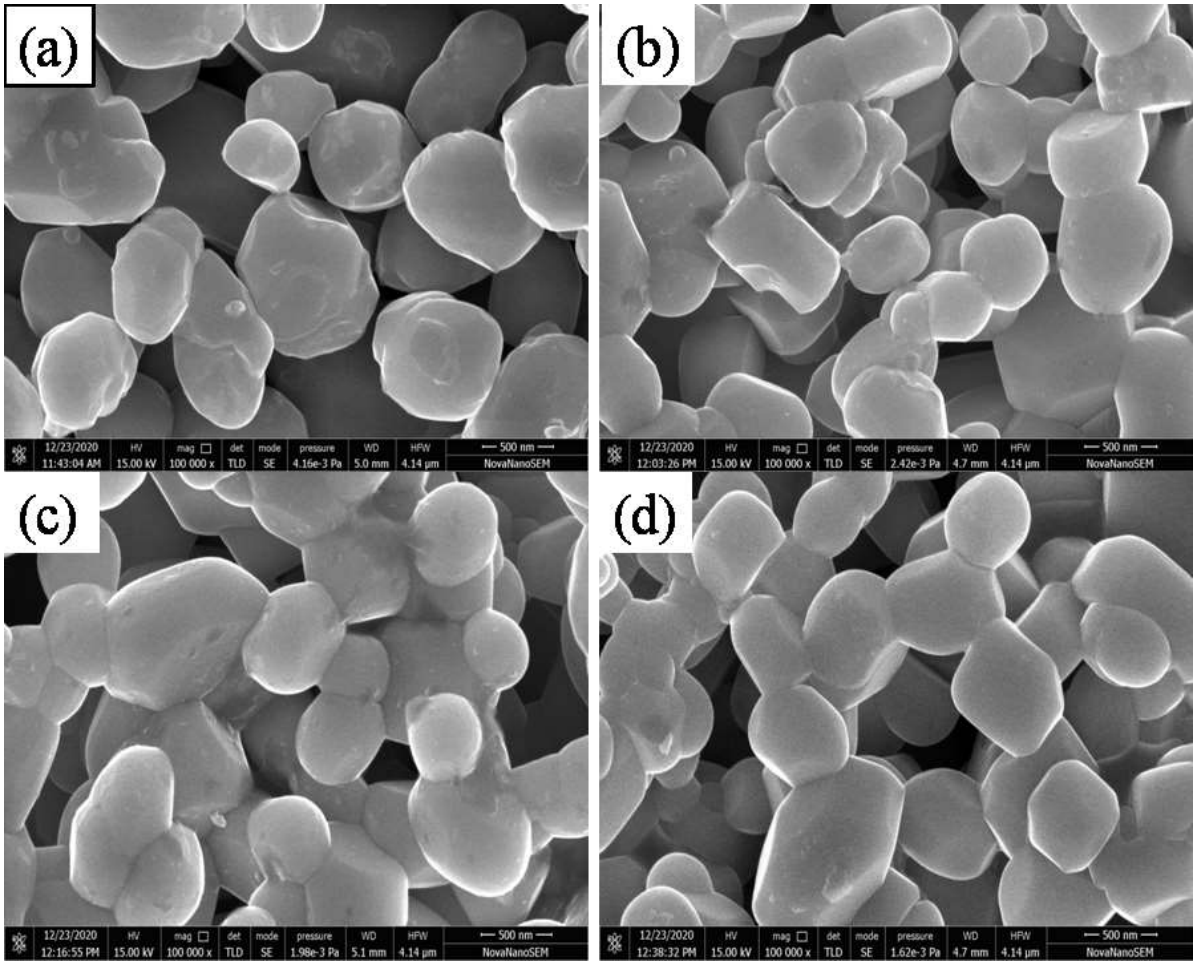

Fig. 3.2. SEM images of (a) BCTO (b) BCMgTO-0.05 (c) BCMgTO-0.1 and (d) BCMgTO-0.2 ceramics

3.3.3. Transmission Electron Microscopic (TEM) studies

The bright-field TEM image of BCMgTO-0.2 ceramic sintered at 1173 K for 8 h is shown in fig. 3.3a.The TEM image confirms that the BCTO ceramic possesses crystalline particles of cubical shape. The particle size was observed by TEM analysis with the help of Image-J software and was found to be 102.6 nm for BCMgTO-0.2 ceramic. Fig.3.3b displays the Selected Area Electron Diffraction (SAED) pattern of BCMgTO-0.2 ceramic. We have indicated the crystal plane the SAED pattern of the ceramic.

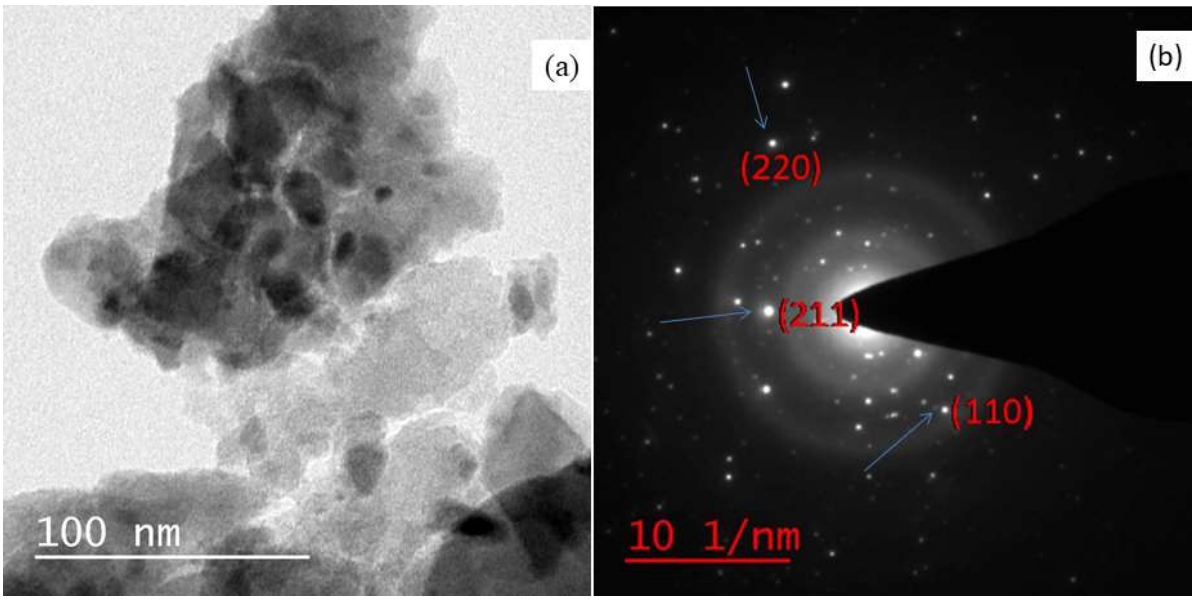

Fig. 3.3. Bright-field TEM image; b SAED pattern of BCMgTO-0.2 ceramic sintered at 1173 K for 8 h.

The occurrence of few clear rings with small dots in the SAED pattern confirms the formation of polycrystalline Mg-doped BCTO ceramic.

3.3.4. X-ray photoelectron spectroscopic (XPS) studies

Fig. 3.4(a)-(e) shows the XPS spectrum of BCMgTO-0.2 ceramic. For this analysis, Carbon 1s was taken as a reference, which has assigned B.E. value 284.6eV to account for the charge effects of the surface. Fig. 3.4(b) depicts the XPS spectrum of Bi in BCMgTO-0.2 ceramic. Two values were achieved $^4f_{5/2}$ and $^4f_{7/2}$, whose corresponding B.E. values were 158.8 eV and 164.1 eV. The above result confirmed that bismuth ion exists in the +3 oxidation state in BCMgTO-0.2 ceramic. The binding energy peak was found to be at 1303.6 eV and 1304.4 eV for Mg 1s lower and higher respectively, which is shown in Fig.3.4(c). The above result confirmed the existence of a +2 oxidation state of Mg ion in the ceramic. Fig. 3.4(a) depicts the XPS spectrum of Copper in BCMgTO-0.2 ceramic. The binding energy of copper in BCMgTO-0.2 ceramic confirmed the existence of a +2 oxidation state of Cu with the binding energy related to Cu ^2p spectra at the peak of 933.9 eV and 953.6 eV that corresponds to Cu

$^2p_{3/2}$ and Cu $^2p_{1/2}$, respectively [36].

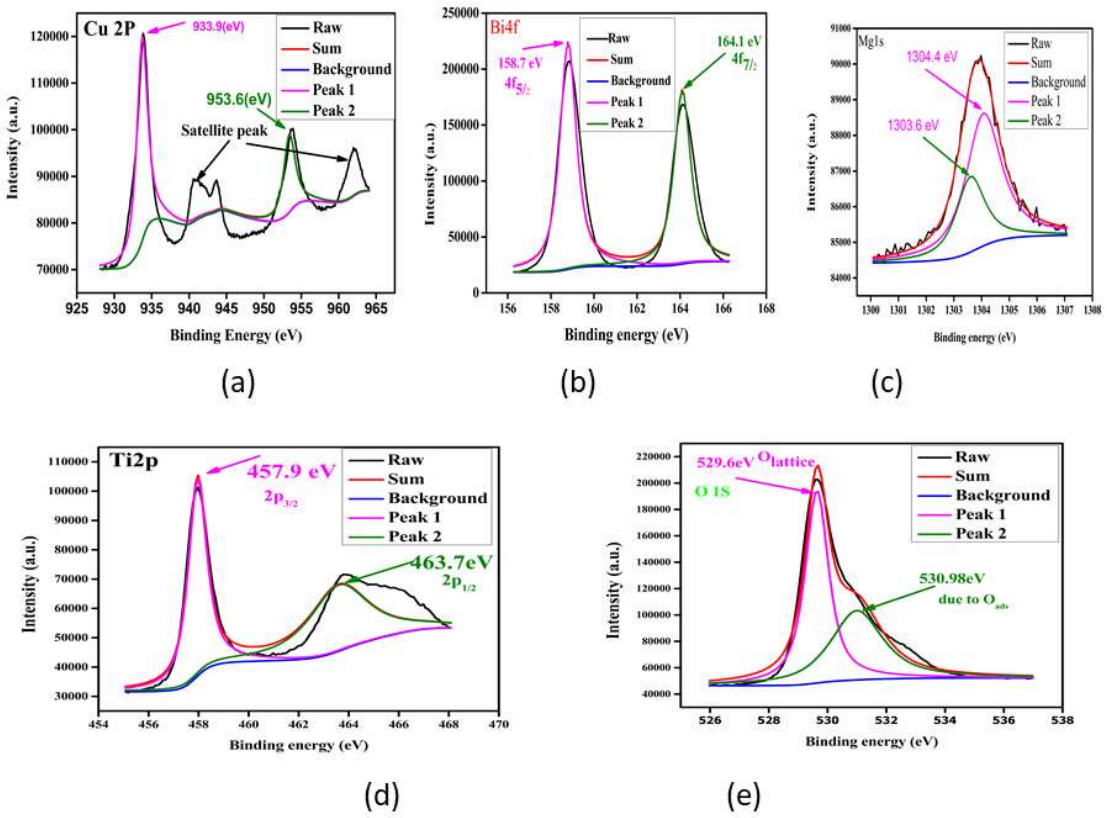

Fig. 3.4. XPS spectra of (**a)** Cu (**b)** Bi, (**c)** Mg; (**d)** Ti; **e** O of BCMgTO-0.2 ceramic sintered at 1173 K for 8 h.

Fig. 3.4(d) depicts the XPS spectrum of BCMgTO-0.2 ceramic at 457.9 eV, 463.7 eV which corresponding to the Ti ^2p doublet namely Ti $^2p_{3/2}$ and Ti $^2P_{1/2}$ confirmed the presence of +4 oxidation state of Ti ion [37]. The binding energy peak of Oxygen of BCMgTO-0.2 ceramic was found to be 529.6 eV and 530.9 eV correspondings to lower and higher binding energy is shown in Fig. 3.4(e). The above result confirmed the presence of a +2 oxidation state of

Oxygen ion in BCMgTO-0.2 ceramic. Thus, all ions present in the ceramic were found in the required oxidation states, which was confirmed by XPS studies.

3.3.5. Dielectric studies

Fig. 3.5a displays the frequency dependence of ε_r for sintered Mg-doped and undoped BCTO ceramics at 303 K. The value of ε_r for BCTO, BCMgTO-0.05, BCMgTO-0.1, and BCMgTO-0.2 ceramics were found to be 3024, 325, 800, and 200 respectively at 423 K and 100 Hz. High ε_r~2.52×10^4 at room temperature and 1 kHz were accomplished in the $CaCu_{2.9}Mg_{0.1}Ti_4O_{12}$ (CCMgTO-0.1) ceramic sintered at 1353 K for 8 h [38].The dielectric constant (ε_r) decreases rapidly in the lower frequency range whereas, in the higher frequency range, It decreases slowly as shown in fig. 3.5a. Fig. 3.5b shows the variation of tangent loss (tan δ) with frequency at 303 K. It is obvious from the figure that the value of tan δ decreases with an increase in frequency in lower frequency regions, while it decreases smoothly in the higher frequency region.

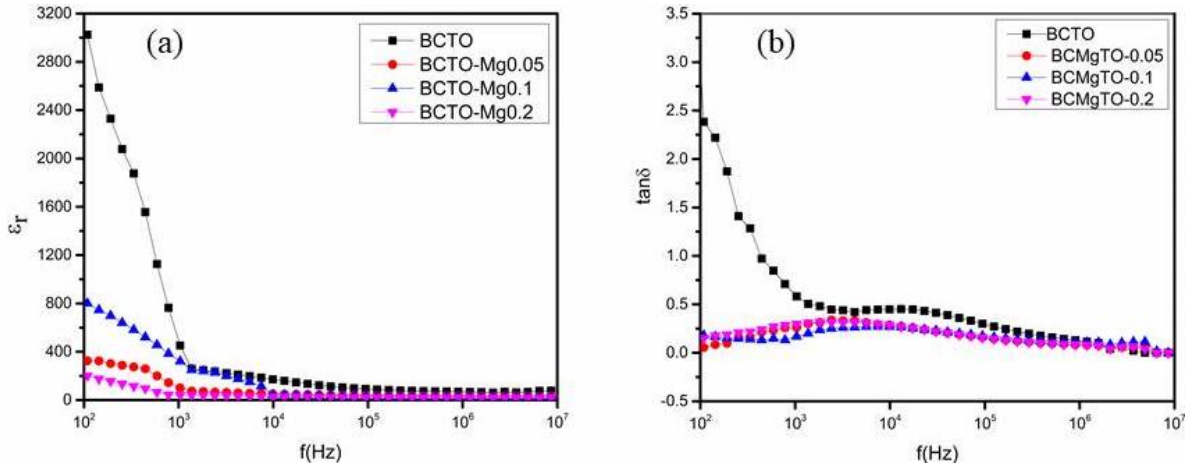

Fig. 3.5. Frequency dependence of (**a**) dielectric constant(ε_r); (**b**) dielectric loss (tan δ) for BCTO, BCMgTO-0.05, BCMgTO-0.1, and BCMgTO-0.2 ceramics sintered at 1173 K for 8 h.

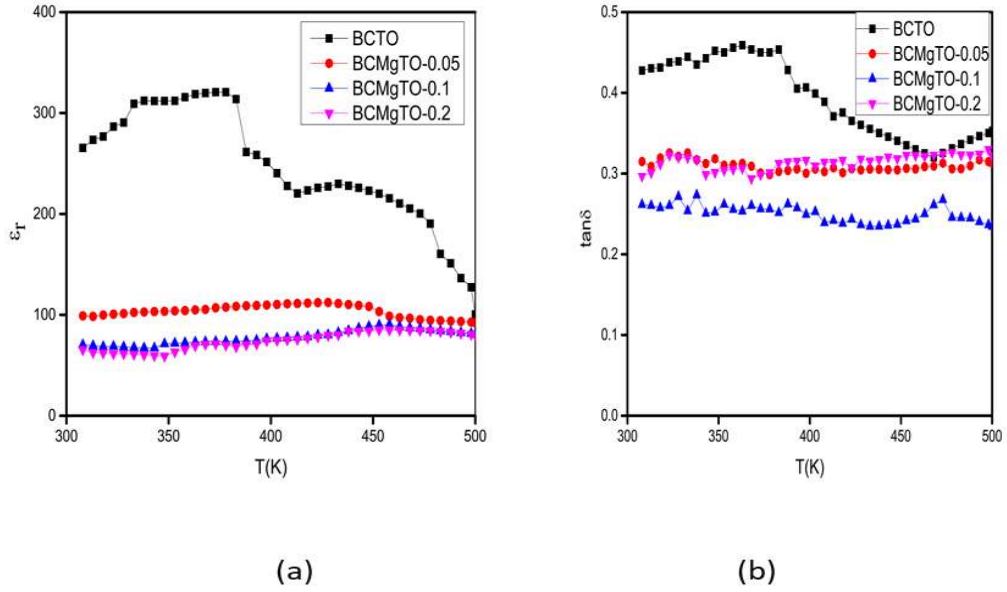

Fig. 3.6. Temperature dependence of (**a**) dielectric constant(ε_r); (**b**) tangent loss (tan δ) of BCTO, BCMgTO-0.05, BCMgTO-0.1; BCMgTO-0.2 ceramics sintered at 1173 K for 8 h.

The dielectric loss of BCTO, BCMgTO-0.05, BCMgTO-0.1, and BCMgTO-0.2 ceramics was found to be 0.45, 0.27, 0.26, and 0.28 respectively at 303 K and 10 kHz. Fig. 3.6a and fig.3.6b displays the variation of ε_r and tangent loss with the temperature at 10 kHz frequency. It is noted from the figure that the value of ε_r and tan δ first increases, attains a maximum, and then decreases slowly to a lower value. The variations of ε_r and tan δ are

qualitatively analogous showing dielectric distribution at lower frequencies. Both show a decrease and then become nearly independent of frequency. This type of frequency behavior can be described based on the space charge model of Maxwell-Wagner [39].

3.3.6. Impedance spectroscopic studies

The complex impedance plot (Z″ vs Z′) of Mg-doped and un-doped BCTO ceramics sintered at 1173 K for 8 h at 303 K is shown in fig.3.7a.The figure reveals the presence of semicircular arcs with different intercepts, which may be due to the grain and grain boundaries contribution in higher frequency, and no contribution due to electrode specimens is observed in this frequency range. The arcs for grains at high frequency get suppressed due to the high value of grain boundary resistance, which is usually observed for IBLC, a characteristic of semiconducting grain with insulating grain boundaries. Thus, the dielectric property of BCTO ceramics (Mg-doped and non-doped) is due to the combined effect of grain and grain boundary. The variation of the imaginary part of impedance (Z″) and the real part of impedance (Z′) with frequency at 303K is shown in fig. 3.7b and fig. 3.7c respectively.

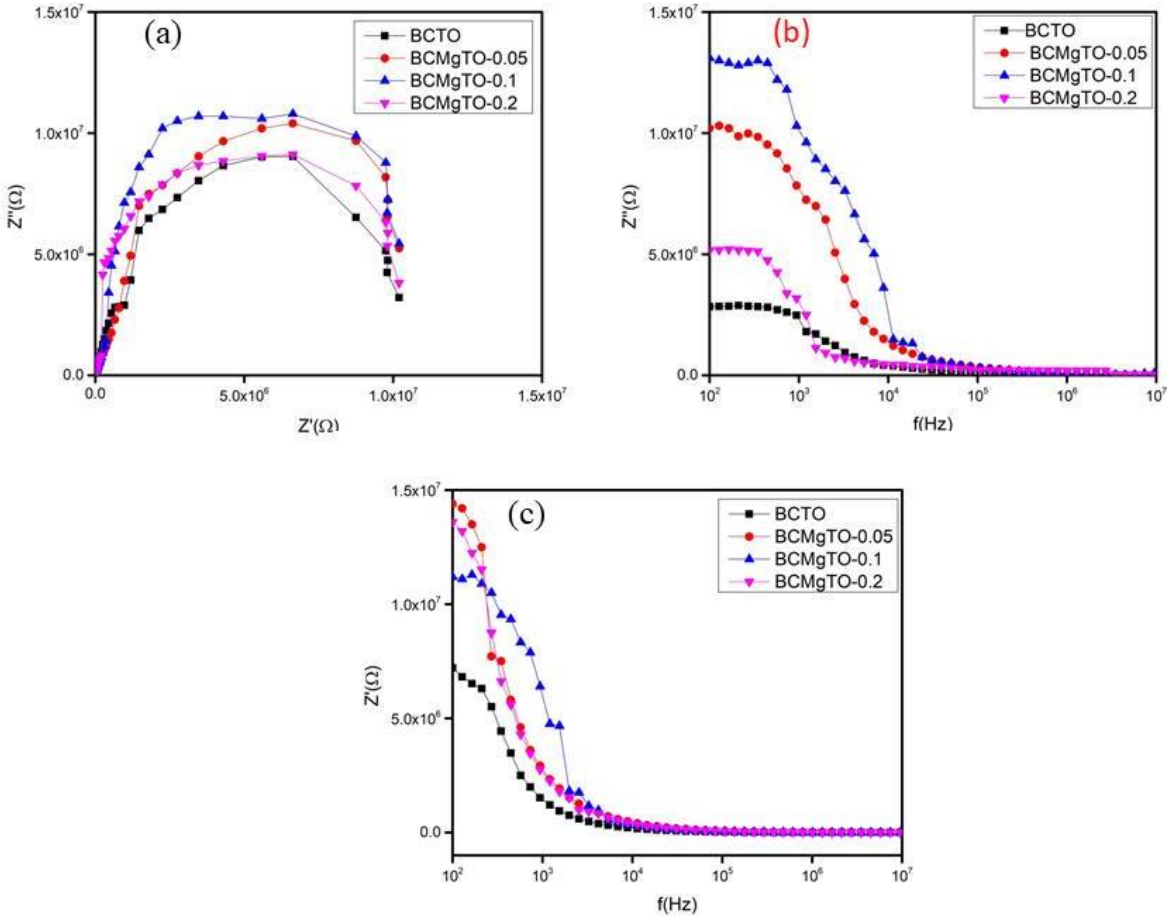

Fig. 3.7. (a) Complex impedance plot or cole-cole plot (Z″ vs Z′), (**b)** frequency dependence of imaginary part of impedance (Z″) and (**c)** frequency dependence of real part of impedance (Z′) at 303 K for BCTO, BCMgTO-0.05, BCMgTO-0.1 and BCMgTO-0.2 ceramics.

It shows the appearance of relaxation peaks. [40-42]. The peak relaxation was observed at a lower frequency and peak suppression occurred at a high frequency, which confirms the presence of the relaxation phenomenon of $Bi_{2/3}Cu_3Ti_4O_{12}$ ceramics.

3.3.7. Conductivity measurements:-

Conductivity is calculated by the following formula

$$\sigma = \frac{1}{R}.\left(\frac{l}{A}\right) \quad (3.2)$$

Where σ is conductivity, R is the grain boundary resistance (ohm), l is the thickness of the ceramic and A is the area of the electrode.

The variation of ln of conductivity (σ) as a function of 1000/T (K^{-1}) at 10 kHz frequency for Mg-doped and undoped BCTO ceramics sintered at 1173 K for 8 h, is shown in Fig. 3.8a.

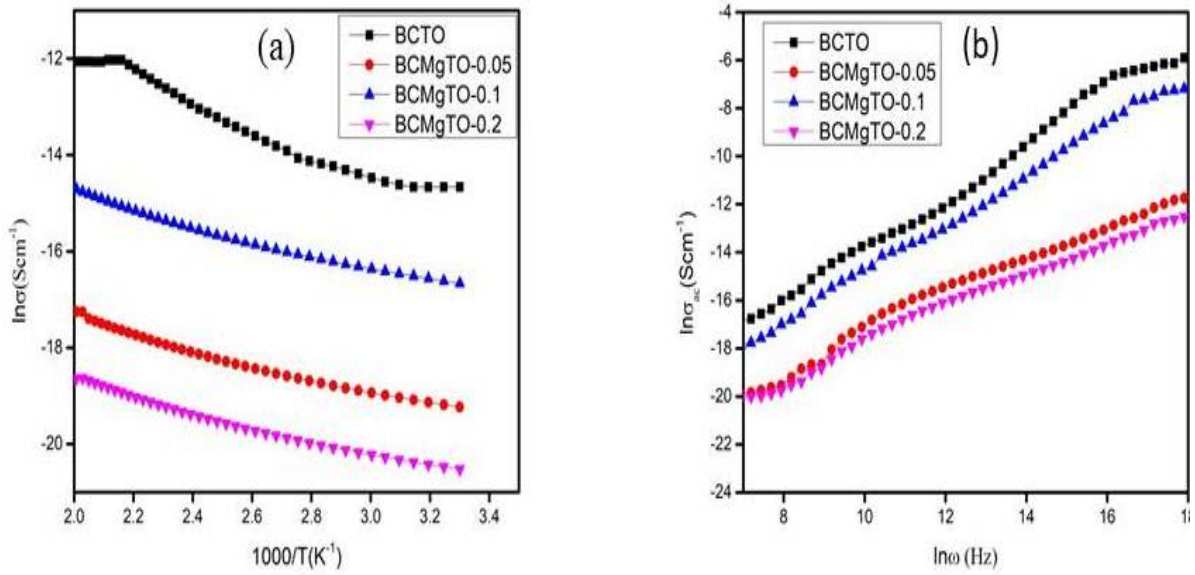

Fig. 3.8. (a) Plots of conductivity (ln σ) with the inverse of temperature at 10 kHz; **(b)** frequency dependence of AC conductivity at 303K for BCTO, BCMgTO-0.05, BCMgTO-0.1 and BCMgTO-0.2 ceramics.

It is observed from the figure that the value of ln σ decreases with a decrease in temperature. Meanwhile, the conductivity (σ) obeys the Arrhenius law

$$\sigma = \sigma 0 e^{-Ea/\mathrm{kB}T} \quad (3.3)$$

Where σ is the conductivity at the given temperature T, σ_0 is the pre-exponent factor, E_a is the activation energy, k_B is Boltzmann constant and T is the absolute temperature in K. The following relation with ln σ and 1/T can be obtained by equation (3.4).

$$\ln \sigma = \ln \sigma_0 - E_a / k_B T \quad (3.4)$$

Where as conduction activation energy. Conduction activation energy is calculated by the slope of the plot of ln σ vs 1000/T. The calculated conduction activation energy values for BCTO, BCMgTO-0.05, BCMgTO-0.1 and BCMgTO-0.2 ceramics are 0.27eV, 0.16 eV, 0.14 eV and 0.13 eV respectively. It should be noted that, by Mg doping in BCTO ceramic, its conduction activation energy decreases.

The frequency-dependent conductivity can be described by Johncher's power law, which is given by [43],

$$\sigma(\omega) = \sigma_0 + A\omega^s \quad (3.5)$$

Where A is a constant and s is the power-law exponent, $0 < s < 1$.

The transport mechanism (Conductivity Phenomenon) is explained by the thermally activated hopping process between two sites separated by an energy barrier. AC conductivity [43, 44] mainly depends upon frequency. The variation of AC conductivity with frequency is shown in Fig. 3.8b. The value of Power-law exponent(s) was calculated by the slope of $\ln\sigma_{ac}$ vs $\ln \omega$. It was calculated to be 0.94, 0.89, 0.64 and 0.65 for BCTO, BCMgTO-0.05, BCMgTO-0.1 and BCMgTO-0.2 ceramics respectively.

3.4. Conclusions

Mg-doped and un-doped BCTO ceramics were successfully synthesized via a semi-wet method using metal acetate, metal nitrate solutions, and solid TiO_2 powder. BCTO phase formation was confirmed by XRD. The crystallite size of Mg-doped and non-doped BCTO ceramics were found to be in the range of 35-47 nm by XRD. The particle size of BCMgTO-0.2 ceramic (higher Mg-doped sample) was found to be 102.6 nm by TEM studies. The average grain size of BCTO, BCMgTO-0.05, BCMgTO-0.1, and BCMgTO-0.2 was found 0.70 μm, 0.63 μm, 0.60 μm and 0.57 μm respectively. The oxidation state was confirmed by XPS. At low frequency, a high value of dielectric constant (ε_r) and at high frequency, low tangent losses were recorded. The impedance and Modulus analysis of BCTO ceramics confirmed the presence of the phenomenon of grain and grain boundaries effects. The conductivity of BCTO ceramics increases with an increase in temperature obeying the Arrhenius law. AC conductivity of BCTO ceramics increases with increasing frequency satisfying Johncher's power law.

References:

1. Pandey, S., Kumar, A., Singh, N.B. and Mandal, K.D. (2020). Studies on dielectric and magnetic properties of $CaCu_3Ti_3MnO_{12}$ ceramic synthesized via semi-wet route. *Journal of the Australian Ceramic Society*, 56, 915-922.

2. Li, M., Cai, G., Zhang, D.F., Wang, W.Y., Wang, W.J. and Chen, X.L. (2008). Enhanced dielectric responses in Mg-doped $CaCu_3Ti_4O_{12}$. *Journal of Applied Physics*, *104*(7), 074107.

3. Zhang, J., Li, Z., Liu, Y., Zheng, J., Lu, W., Guo, S., Lei, Z., Lin, L. and Tian, M. (2020). Enhanced dielectric properties of CCTO ceramics doped by different halogen elements. *Journal of Materials Science: Materials in Electronics*, 31, 8481-8488.

4. Mao, P., Wang, J., Liu, S., Zhang, L., Zhao, Y. and He, L. (2019). Grain size effect on the dielectric and non-ohmic properties of $CaCu_3Ti_4O_{12}$ ceramics prepared by the sol-gel process. *Journal of Alloys and Compounds*, 778, 625-632.

5. Subramanian, M.A., Li, D., Duan, N., Reisner, B.A. and Sleight, A.W. (2000). High dielectric constant in $ACu_3Ti_4O_{12}$ and $ACu_3Ti_3FeO_{12}$ phases. *Journal of Solid State Chemistry*, *151*(2), 323-325.

6. Gaâbel, F., Khlifi, M., Hamdaoui, N., Beji, L., Taibi, K. and Dhahri, J. (2019). Microstructural, structural and dielectric analysis of Ni-doped $CaCu_3Ti_4O_{12}$ ceramic with low dielectric loss. *Journal of Materials Science: Materials in Electronics*, 30, 14823-14833.

7. Tang, Z., Wu, K., Li, J. and Huang, S. (2020). Optimized dual-function varistor-capacitor ceramics of core-shell structured $xBi_{2/3}Cu_3Ti_4O_{12}/(1-x)CaCu_3Ti_4O_{12}$ composites. *Journal of the European Ceramic Society*, 40(9), 3437-3444.

8. Wu, M., Zhang, Y. and Xiang, M. (2019). Synthesis, characterization and dielectric properties of a novel temperature stable $(1- x)CoTiNb_2O_{8-x}ZnNb_2O_6$ ceramic. *Journal of Advanced Ceramics*, 8, 228-237.

9. Sharma, S., Yadav, S.S., Singh, M.M. and Mandal, K.D. (2014). Impedance spectroscopic and dielectric properties of nanosized $Y_{2/3}Cu_3Ti_4O_{12}$ ceramic. *Journal of Advanced Dielectrics*, 4(04), 1450030.

10. Islam, S.A.U., Andrabi, F.A., Mohmed, F., Sultan, K., Ikram, M. and Asokan, K. (2020). Ba doping induced modifications in the structural, morphological and dielectric properties of double perovskite La_2NiMnO_6 ceramics. *Journal of Solid State Chemistry*, 290, 121597.

11. Liu, P., Lai, Y., Zeng, Y., Wu, S., Huang, Z. and Han, J. (2015). Influence of sintering conditions on microstructure and electrical properties of $CaCu_3Ti_4O_{12}$ (CCTO) ceramics. *Journal of Alloys and Compounds*, *650*, 59-64.

12. Yadav, A. K., Fan, H., Yan, B., Wang, W., Dong, W. and Wang, S. (2021). Structure evolutions with enhanced dielectric permittivity and ferroelectric properties of $Ba(_{1-x})(La,Li)_xTiO_3$ ceramics. *Journal of Materials Science: Materials in Electronics*, 32(18), 23103-23115.

13. West, A.R., Adams, T.B., Morrison, F.D. and Sinclair, D.C. (2004). Novel high capacitance materials:-$BaTiO_3$: La and $CaCu_3Ti_4O_{12}$. *Journal of the European Ceramic Society*, 24(6), 1439-1448.

14. Wu K., Huang Y., Lia J. and Li S. (2017). Space charge polarization modulated instability of low frequency permittivity in $CaCu_3Ti_4O_{12}$ ceramics. *Applied Physics Letter*, 111, 042902.

15. Adams, T.B., Sinclair, D.C. and West, A.R. (2002). Giant barrier layer capacitance effects in $CaCu_3Ti_4O_{12}$ ceramics. *Advanced Materials*, 14(18), 1321-1323.

16. Riquet, G., Marinel, S., Bréard, Y. and Harnois, C. (2019). Sintering mechanism and grain growth in $CaCu_3Ti_4O_{12}$ ceramics. *Ceramics International*, 45(7), 9185-9191.

17. Homes, C.C., Vogt, T., Shapiro, S.M., Wakimoto, S., Subramanian, M.A. and Ramirez, A.P. (2003). Charge transfer in the high dielectric constant materials $CaCu_3Ti_4O_{12}$ and $CdCu_3Ti_4O_{12}$. *Physical Review B*, 67(9), 092106.

18. Hadi, N., Lamcharfi, T., Abdi, F., Echtoui, N.S., Harrach, A., Zouhairi, M. and Ahjyaje, F.Z. (2019). The effects of calcination and doping on structural and dielectric properties of $CaCu_{3-x}Co_xTi_4O_{12}$ ceramic. *Mediterranean Journal of Chemistry*, 8(3), 234-244.

19. Zhao, C. and Wu, J., 2018. Effects of secondary phases on the high-performance colossal permittivity in titanium dioxide ceramics. *ACS applied materials & interfaces*, 10(4), 3680-3688.

20. Rani, S., Ahlawat, N., Punia, R., Sangwan, K.M. and Khandelwal, P. (2018). Dielectric and impedance studies of La and Zn co-doped complex perovskite $CaCu_3Ti_4O_{12}$ ceramic. *Ceramics International*, 44(18), 23125-23136.

21. Yang, L., Huang, G., Wang, T., Hao, H. and Tian, Y. (2016). Colossal dielectric permittivity and relevant mechanism of $Bi_{2/3}Cu_3Ti_4O_{12}$ ceramics. *Ceramics International*, 42(8), 9935-9939.

22. Liu, J., Duan, C.G., Yin, W.G., Mei, W.N., Smith, R.W. and Hardy, J.R. (2004). Large dielectric constant and maxwell-wagner relaxation in $Bi_{2/3}Cu_3Ti_4O_{12}$. *Physical review B*, 70(14), 144106.

23. Deng, J., Sun, X., Liu, S., Liu, L., Yan, T., Fang, L. and Elouadi, B. (2016). Influence of interface point defect on the dielectric properties of Y doped $CaCu_3Ti_4O_{12}$ ceramics. *Journal of advanced dielectrics*, 6(01), 1650009.

24. Li, W. and Schwartz, R.W. (2007). Derivation and application of an empirical formula to describe interfacial relaxation effects in inhomogeneous materials. *Journal of the American Ceramic Society*, 90(11), 3536-3540.

25. De Almeida-Didry, S., Nomel, M.M., Autret, C., Honstettre, C., Lucas, A., Pacreau, F. and Gervais, F., 2018. Control of grain boundary in alumina doped CCTO showing colossal permittivity by core-shell approach. *Journal of the European Ceramic Society*, 38(9), 3182-3187.

26. Xu, J., Hassan, D.A., Zeng, R.J. and Peng, D.L. (2016). $Lu_3Al_5O_{12}$: Ce@SiO_2 phosphor-in-glass: its facile synthesis, reduced thermal/chemical degradation and application in high-power white LEDs. *Journal of the European Ceramic Society*, 36(8), 2017-2025.

27. Schmidt, R., Stennett, M.C., Hyatt, N.C., Pokorny, J., Prado-Gonjal, J., Li, M. and Sinclair, D.C. (2012). Effects of sintering temperature on the internal barrier layer capacitor (IBLC) structure in $CaCu_3Ti_4O_{12}$ (CCTO) ceramics. *Journal of the European Ceramic Society*, 32(12), 3313-3323.

28. Lin, H., Xu, W., Zhang, H., Chen, C., Zhou, Y. and Yi, Z. (2020). Origin of high dielectric performance in fine grain-sized $CaCu_3Ti_4O_{12}$ materials. *Journal of the European Ceramic Society*, 40(5), 1957-1966.

29. Capsoni, D., Bini, M., Massarotti, V., Chiodelli, G., Mozzatic, M.C. and Azzoni, C.B. (2004). Role of doping and CuO segregation in improving the giant permittivity of $CaCu_3Ti_4O_{12}$. *Journal of Solid State Chemistry*, 177(12), 4494-4500.

30. Li, M., Shen, Y. and Li, C.X. (2019). Study of the dielectric properties of $ACu_3Ti_4O_{12}$ (A= $Eu_{2/3}$, $Tb_{2/3}$, and $Na_{1/2}Eu_{1/2}$). *Powder Diffraction*, 34(4), 345-351.

31. Bender, B.A. and Pan, M.J. (2005). The effect of processing on the giant dielectric properties of $CaCu_3Ti_4O_{12}$. *Materials Science and Engineering: B*, 117(3), 339-347.

32. Pandey, S., Kumar, V. and Mandal, K.D. (2020). Studies of sintering temperature on the microstructure, magnetic and dielectric behavior of $CaCu_3Ti_{3.5}Mn_{0.5}O_{12}$ ceramic synthesized by semi-wet route. *SN Applied Sciences*, 2, 1-9.

33. Löhnert, R., Schmidt, R. and Töpfer, J. (2015). Effect of sintering conditions on microstructure and dielectric properties of $CaCu_3Ti_4O_{12}$ (CCTO) ceramics. *Journal of electroceramics*, 34, 241-248.

34. Li, M., Sinclair, D.C. and West, A.R. (2011). Extrinsic origins of the apparent relaxor like behavior in $CaCu_3Ti_4O_{12}$ ceramics at high temperatures: a cautionary tale. *Journal of Applied Physics*, 109(8). 084106.

35. Jumpatam, J., Putasaeng, B., Chanlek, N., Kidkhunthod, P., Thongbai, P., Maensiri, S. and Chindaprasirt, P. (2017). Improved giant dielectric properties of $CaCu_3Ti_4O_{12}$ via simultaneously tuning the electrical properties of grains and grain boundaries by F^- substitution. *RSC Advances*, 7(7), 4092-4101.

36. Jaiswar, S. and Mandal, K.D. (2017). Evidence of enhanced oxygen vacancy defects inducing ferromagnetism in multiferroic $CaMn_7O_{12}$ manganite with sintering time. *The Journal of Physical Chemistry C*, 121(36), 19586-19601.

37. Han, C.S., Choi, H.R., Choi, H.J. and Cho, Y.S. (2017). Origin of abnormal dielectric behavior and chemical states in amorphous $CaCu_3Ti_4O_{12}$ thin films on a flexible polymer substrate. *Chemistry of Materials*, 29(14), 5915-5921.

38. Sun, L., Zhang, R., Wang, Z., Cao, E., Zhang, Y. and Ju, L. (2016). Microstructure and enhanced dielectric response in Mg doped $CaCu_3Ti_4O_{12}$ ceramics. *Journal of Alloys and Compounds*, 663, 345-350.

39. Godara, P., Agarwal, A., Ahlawat, N. and Sanghi, S. (2018). Crystal structure, dielectric and magnetic properties of Gd doped $BiFeO_3$ multiferroics. *Physica B: Condensed Matter*, 550, 414-419.

40. Howell, F.S., Bose, R.A., Macedo, P.B. and Moynihan, C.T. (1974). Electrical relaxation in a glass-forming molten salt. *The Journal of Physical Chemistry*, 78(6), 639-648.

41. Salah, M., Azizi, S., Boukhachem, A., Khaldi, C., Amlouk, M. and Lamloumi, J. (2019). Rietveld refinement of X-ray diffraction, impedance spectroscopy and dielectric relaxation of Li-doped ZnO-sprayed thin films. *Applied Physics A*, 125, 1-21.

42. Costa, M.M., Pires, G.F.M., Terezo, A.J., Graca, M.P.F. and Sombra, A.S.B. (2011). Impedance and modulus studies of magnetic ceramic oxide $Ba_2Co_2Fe_{12}O_{22}$ (Co_2Y) doped with Bi_2O_3. *Journal of Applied Physics*, 110(3), 034107.

43. Adnan, S.B.R.S. and Mohamed, N.S., 2014. AC conductivity and dielectric studies of modified Li_4SiO_4 ceramic electrolytes. *Ceramics International*, 40(7), 11441-11446.

44. Yu, K., Tian, Y., Gu, R., Jin, L., Ma, R., Sun, H., Xu, Y., Xu, Z. and Wei, X. (2018). Ionic conduction, colossal permittivity and dielectric relaxation behavior of solid electrolyte $Li_{3-x}La_{2/3-x}TiO_3$ ceramics. *Journal of the European Ceramic Society*, *38*(13), 4483-4487.